MOF-derived Robust and Synergetic Acid Sites Inducing C-N Bond Disruption for Energy-Efficient CO_2 Desorption

Lei Xing[1,2,†], Meng Li [1, †], Mingyue Li[1], Teng Xu[1], Yuchen Li[1], Tieyue Qi[1], Huanxin Li[3], Zhigang Hu[3], Guang-ping Hao[4], Shihan Zhang[5], Tony David James[6], Boyang Mao[3,], and Lidong Wang[1,*]*

[1] MOE Key Laboratory of Resources and Environmental Systems Optimization, College of Environmental Science and Engineering, North China Electric Power University, Beijing, 102206, PR China

[2] State Key Joint Laboratory of Environment Simulation and Pollution Control, School of Environment, Tsinghua University, Beijing 100084, PR China

[3] Department of Engineering, University of Cambridge, Cambridge, CB3 0FA, UK

[4] State Key Laboratory of Fine Chemicals, Liaoning Key Laboratory for Catalytic Conversion, Carbon Resources, College of Environment, School of Chemical Engineering, Dalian University of Technology, Dalian, 116024, P. R. China

[5] College of Environment, Zhejiang University of Technology, Hangzhou, 310014, P. R. China

[6] Prof. Tony David James, Department of Chemistry, University of Bath, Bath, BA2 7AY, UK

[†] These authors contributed equally to this work

[*] Corresponding authors. E-email: wld@ncepu.edu.cn and maoboyang@gmail.com

Abstract: Amine-based scrubbing technique is recognized as a promising method of capturing CO_2 to alleviate climate change. However, the less stability and poor acidity of solid acid catalysts (SACs) limit its potential to further improve amine regeneration activity and reduce the energy penalty. To address these challenges, here, we introduce two-dimensional (2D) cobalt-nitrogen-doped carbon nanoflakes (Co–N–C NSs) driven by a layered metal organic framework that work as SACs. The designed 2D Co–N–C SACs can exhibit promising stability, super-hydrophilic surface, and acidity. Such 2D structure also contain well-confined Co–N_4 Lewis acid sites and –OH Brønsted acid sites to have a synergetic effect on C-N bond disruption and significantly increase CO_2 desorption rate by 281% and reduce the reaction temperatures to 88 °C, minimizing water evaporation by 20.3% and subsequent regeneration energy penalty by 71.7% compared to the non-catalysis.

Key words: Solid acid catalyst, 2D nanoflakes, CO_2 capture, MEA regeneration, Energy efficiency

Synopsis: MOF-derived 2D nanoflakes with exceptional catalytic performance was constructed as a robust solid acid catalyst to achieve energy-efficient CO_2 capture.

1. Introduction

Climate change caused by greenhouse gas (GHG) emissions represents an enormous threat to the environment, economy, and society.[1, 2] Reducing global carbon dioxide (CO_2) emissions to net zero by 2050 has become an urgent issue to limit the long-term increase of the average global temperature to within 1.5 °C.[3-5] Given current CO_2 capture and storage (CCS) technologies such as solid sorbent adsorption, membrane separation, and so on, amine-based chemisorption using monoethanolamine (MEA), also known as "amine scrubbing," is one of the most preferred and applicable in a real-world scenario due to its high capacity, maturity, and feasibility in controlling large volumes of CO_2-containing gases from industrial sources.[6-8] In amine scrubbing process, MEA reacts with CO_2 to generate carbamate ($RNHCOO^-$) and bicarbonate (HCO_3^-) in the absorber, which are then regenerated in the desorber. Due to the highly endothermic reaction of N–C bond rupture in $RNHCOO^-$ and restricted proton (RNH_3^+ and H_3O^+) transfer in alkaline solutions, the water-based MEA solvent has to be regenerated at above

110~130 °C to partially compensate for the low CO_2 desorption rate.[9, 10] Such high temperatures require overcoming the latent heat capacity of water, resulting in a regeneration energy penalty of up to 3.5–4.0 GJ/ton CO_2 and making MEA chemisorption technology unsustainable (the regeneration is an indirect source of CO_2 related to the use of fuels).[11, 12] In this respect, reducing the regeneration temperatures for energy-efficient MEA (< 100 °C, the typical temperature for restricting water volatilization) is critical to achieve commercial viable and energy-efficient CO_2 capture.[13]

The application of solid acid catalysts (SACs) has been proposed as an emerging cost-effective strategy to considerably increase CO_2 desorption rates and reduce the regeneration temperature/heat duty in the amine scrubbing process.[14] Typically, the Brønsted acid sites (BASs) present in SACs, such as –OH, $–SO_3H$, and $–HPO_3$, are favorable to serve as proton donors, thus accelerating the proton transfer processes in the CO_2-loaded solvent.[15-17] While Lewis acid sites (LASs), such as the unsaturated Co, Fe, Zr sites, act as electron acceptors for the N and O atoms in $RNHCOO^-$, thus catalyzing the N–C bond rupture processes, further improving the rate of $RNHCOO^-$ decomposition.[18, 19] A higher acid activity of SACs can result in a higher efficiency of proton and electron transfer in the amine solvent.[14] The utilization of SACs, especially state-of- the-art acidified metal oxide (SO_4^{2-}/ZrO_2, SO_4^{2-}/TiO_2, SO_4^{2-}/Fe_3O_4 and SO_4^{2-}/CeO_2) and their molecular sieve composites (SO_4^{2-}/MeO_x-SiO_2/HZSM-5/MCM-41/SBA-15/SAPO-34), contribute towards a significant promotion of proton transfer and decrease of the reaction energy barrier. These efforts enable an increase of MEA regeneration rates approximately 31%~153% while minimizing the heat duty by approximately 10%~30% in comparison with non-catalytic amine regeneration at 98 °C.[20, 21] With our previous research, we demonstrated that cobalt species exhibited a favorable catalytic performance for CO_2 desorption.[22] Compared with the blended amine, biphasic amine and ionic liquid that exhibit higher reaction kinetics while also higher volatility, corrosivity and viscosity, the enhanced desorption rates by SACs enable a reduction of CO_2 desorption temperature and allow the conventional regeneration process to operate at temperatures below 100 °C, which could minimize evaporation energy consumption and prevent MEA degradation.[23, 24] However, the effectiveness of such SACs is limited by their poor specific surface area, pore structure and durability

under treatment with aqueous amine solutions.[14, 25] The three-dimensional hydrophobic surface with small micropore size distribution of the SACs restricts the diffusion of polar reactants ($RNHCOO^-$, RNH_3^+ and H_3O^+) in their to approach active sites.[26] The active protonated sites of BASs are prone to leach in an alkaline environment, and the metal species of LASs will rapidly aggregate with $–NH_2$ groups and removed from activity, thus leading to the deactivation of the SACs.[27] Therefore, although amine regeneration using these SACs can increase the energy efficiency, the inaccessibility and deactivation of the active sites must be suppressed in order to further promote energy-efficient amine regeneration processes. Furthermore, the lowered regeneration temperature is still too high to minimize indirect CO_2 emissions due to the usage of fuels to reach the required temperature, hence there are no benefits to achieving Net Zero.

In previous work, we efficiently pyrolyzed bulk layered metal-organic framework (MOF) precursors and subsequently exfoliated them into 2D cobalt–nitrogen-doped porous carbon nanoflakes (Co–N–C NSs)[28]. The 2D nanoflakes are endowed with exotic reactant diffusion paths, accessible synergetic and multi-functional active sites, and higher hydrophilic surface of host materials. Apparently, robust 2D materials with hydrophilic and acidic surfaces can serve as promising candidates in the design of new SACs.[29, 30] Therefore, rendering this 2D nanoflakes with efficient BASs and LASs is essential to further promote their interaction with $RNHCOO^-$, RNH_3^+ and H_3O^+ guests.

Herein, we designed and exfoliated the 2D Co–N–C NSs with a large lateral size (~ 1μm) and 5 nm thickness. The 2D Co–N–C NSs feature a highly dispersed and uniformly distributed $Co–N_x$ structure, Co^0 nanoclusters and –OH groups. The $Co–N_x$ structure contains unsaturated Co acting as LASs with an electron transfer capacity for $RNHCOO^-$ decomposition; and partial Co^0 nanoclusters can act as magnetic centers to enable magnetic separation providing an economically feasible industrial scale separation process. The introduced –OH containing groups on the 2D nanosheets structure creates a super-hydrophilic surface, which significantly improves the accessibility of reactants to approach the active sites and function as the active BASs to donate protons during the CO_2 desorption processes. The acid rich surface also enables high surface utilization and catalytic efficiency during the CO_2 desorption

processes. Additionally, the strong coordination effect of Co-N_x in Co–N–C NSs restricts the aggregation between Co species with amino groups (–NH), preventing the active components from stripping away from the catalyst surface and providing high stability. Compared to conventional SACs although the concentration of Co–N–C NSs was 0.1wt.% and only 5~10% catalysts usage, Co–N–C NSs achieved a 281% increase in desorption rate of CO_2 at 88 °C and a heat penalty reduction of about 71.7% when compared to standard CO_2 desorption procedures that are around 98°C. This work provides valuable insights into the development of efficient SACs for economically CO_2 capture.

2. Experiments

2.1 Catalyst synthesis

Herein, the Co–N–C NSs as described in our previous work is selected and further modified as SACs for the CO_2 desorption. Typically, taking the etching process of 3D MOF to 2D nanoflakes as an example, Co–N–C NSs was obtained after leaching calcined MOF precursor in 4 M HNO_3 and through centrifugation at 10000 and 1000 rmp, respectively and then freeze-drying.The detailed synthetic method can be founded in Supporting Information.

2.2 Characterization

The techniques such as X-ray photoelectron spectroscopy (XPS), X-ray absorption fine structure (XAFS), Pyridine-adsorption infrared spectroscopy (Py-IR), ammonia temperature–programmed desorption analysis (NH_3-TPD), and one-dimensional (1D) ^{13}C nuclear Magnetic Resonance (NMR) were employed to characterize the catalyst and solvent. Details on characterization methods are given in Supporting Information.

2.3 Catalytic performance evaluation

The rich MEA solvent regeneration experiment was performed by using a simplified batch reactor as previous research[22]. All desorption experiments were conducted under the atmospheric pressure. The quantities of desorbed CO_2 amount from the liquid sample were also measured by gas chromatograph (GC). The CO_2 concentrations and desorption temperature of the CO_2-rich MEA solution was recorded during the CO_2 desorption process. The CO_2 loading of the liquid sample and CO_2 desorption rate were

obtained by converting the measured data from GC workstation. Details on catalytic performance evaluation are exhibited in Supporting Information.

3. Results and Discussion

3.1 Synthesis and characterization of Co–N–C NSs

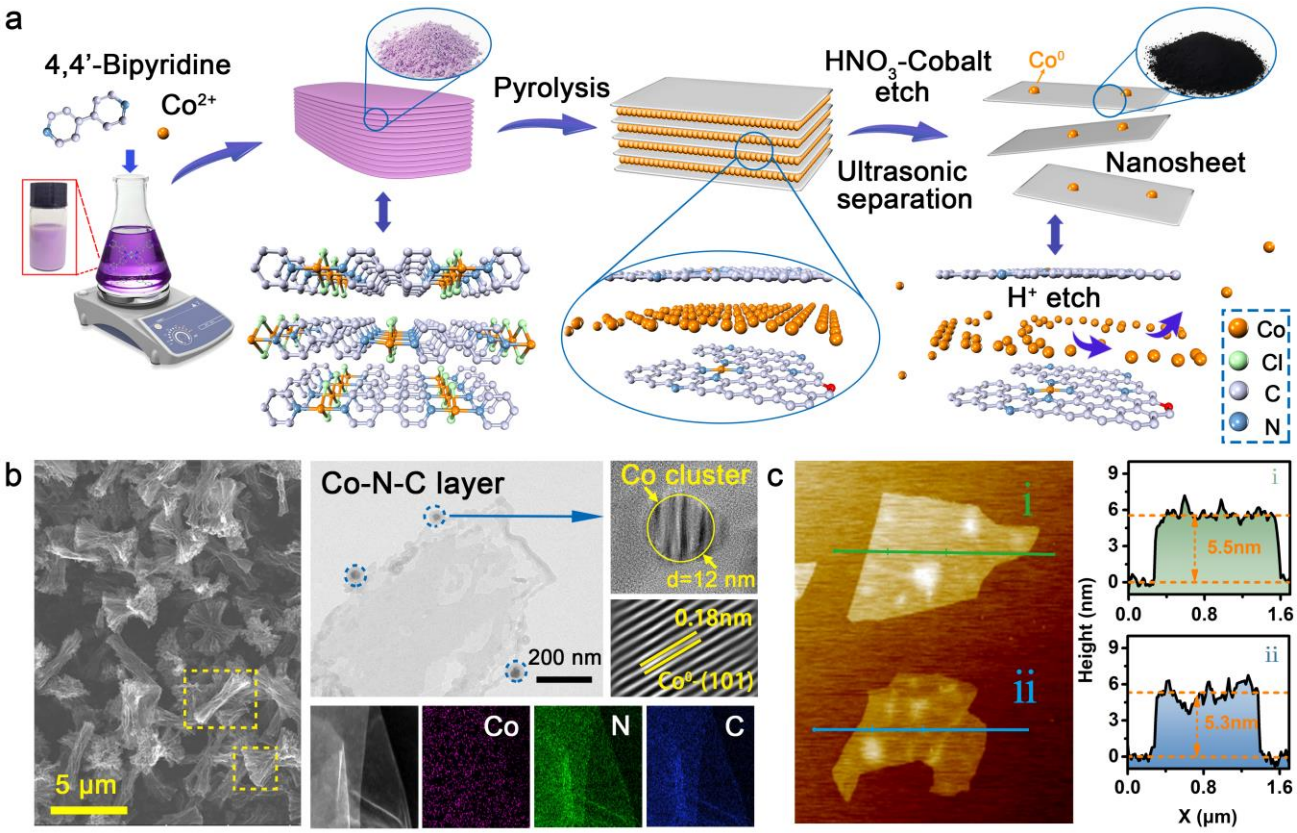

Figure 1. (a) Schematic presentation of the Co–C–N NSs fabrication process; (b) SEM, TEM and Energy-dispersive X-ray spectroscopy (EDX) element mapping images of Co–C–N NSs and (c) ScanAsyst-mode AFM topography of Co–N–C NSs.

The MOF-NSs were selected because the layered MOF structure can be diverse and tailored from an extensive MOF library.[31, 32] The fabrication method of Co–N–C NSs is given in Figure 1a. Using this method, a layered Co-bpy MOF precursor was synthesized from the assembly of 4,4'-bipyridine and cobalt (II) chloride hexahydrate. Scanning electron microscopic (SEM) images (Figure S1) indicated that the Co–bpy possessed a structure containing uniform cylinders stacked with cuboids. Notably, the cobalt species were separated from the nitrogen-containing backbone as carbonization proceeded, leaving the heterocyclic nitrogen rings to fuse and stack around the residual cobalt species. 2D Co–N–C nanoflakes were obtained by using a novel exfoliation strategy *via* metal etching rather than conventional liquid phase

exfoliation that relies on only sonication.[33] As shown in Figure 1a: i) upon carbonization at 500 °C under Argon, the tight layered Co-bpy crystal bundles were transformed into hierarchical Co/N-doped layered porous carbon derivatives, which intercalated with a metallic Co layer (Co–N–C@Co); ii) the microporous and laminated Co–N–C structure was obtained by etching the cobalt metal layer with oxidative HNO_3 acid, and, this acid treatment process could simultaneously introduce abundant oxygen-containing functional groups;[34] iii) the Co–N–C structure was then further exfoliated in isopropyl alcohol to yield Co–N–C NSs with ultra-hydrophilic 2D surfaces.[35] The Co–N–C NSs possessed an open structure comprised of Co–N–C@Co (Figure 1b). More details on the morphology of the prepared catalysts are provided in Figure S1.

The 2D sheet-like Co–N–C NSs nanoflake structure was confirmed using transmission electron microscopic (TEM) images given in Figures 1b and S2. Identical to the TEM observation, the atomic force microscopy (AFM) image in Figure 1c also indicated that the Co–N–C NSs were isolated and depicted a surface morphology of approximately 1 μm lateral size and 5 ± 0.5 nm thickness. The elemental mapping images indicated uniform distributions of Co, N, and C atoms in the Co–N–C NSs layer. Considering the leaching of the partial Co layer might be buffered by the carbon coating layer, the intercalated metallic Co species cannot be completely removed and form Co nanoclusters during the etching process.[36] The Co nanoclusters can be decorated on to the Co–N–C NSs surface with a size of about 12 nm. The Co nanoclusters' interplanar distance was measured to be ~0.18 nm, matching the d-spacing of (101) planes of metallic Co^0, which confirmed a well crystalized Co structure.[37] The X-ray diffraction (XRD) pattern, Figure 2a, exhibited characteristic diffraction peaks at approximately 26.3°, 44.4°, and 47.5°, which were assigned to the typical (002) interlayer from graphite carbon and Co nanoclusters (111 and 101) planes, respectively.[38, 39] The average size of the Co nanoclusters calculated using the Scherrer equation were 11.8 nm, in agreement with the TEM and mapping results.

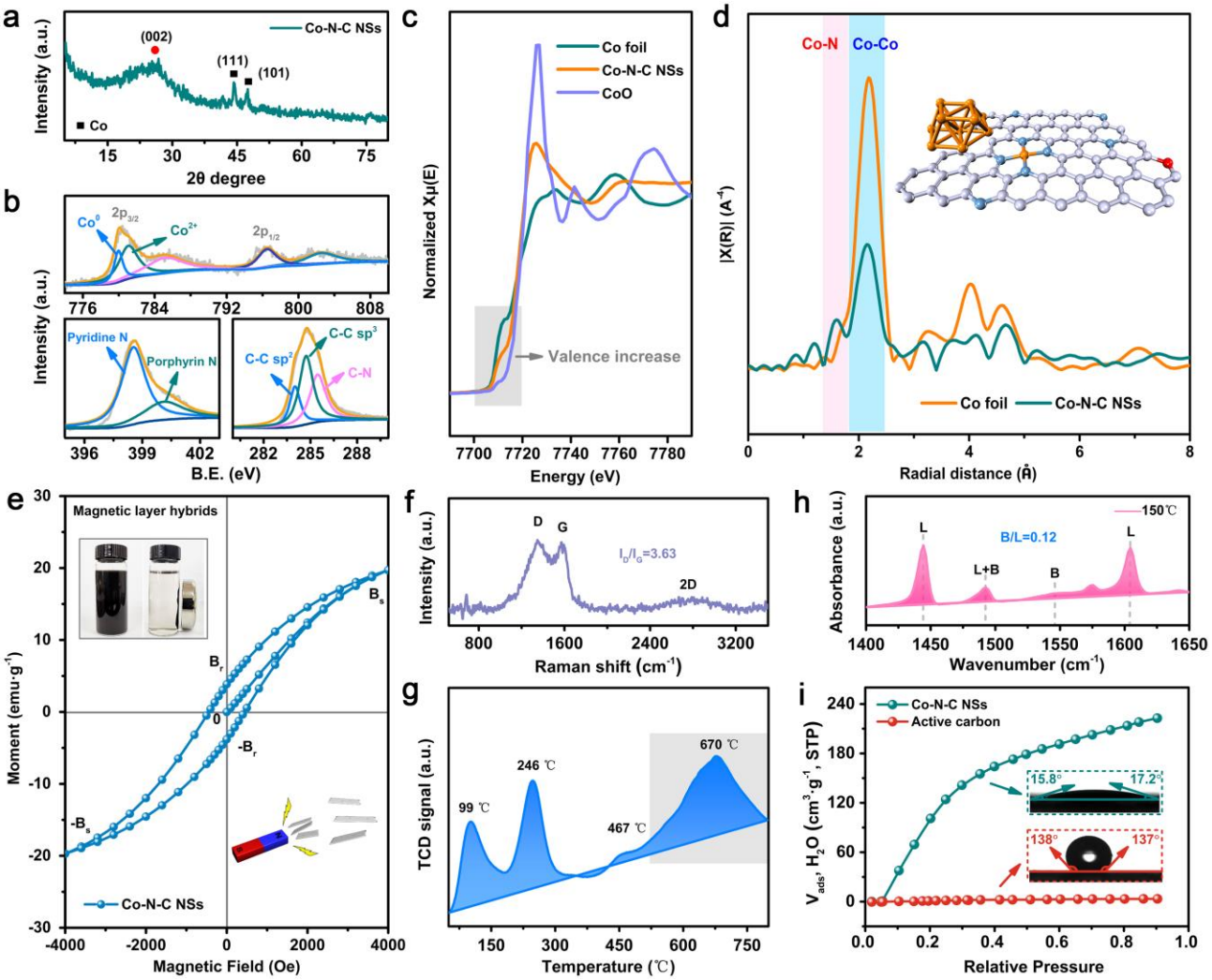

Figure 2. Structural characterization of Co–N–C NSs catalyst: (a) XRD pattern; (b) XPS spectra of Co 2p, N 1s, and C 1s; (c) Co K-edge XANES and (d) Fourier transform EXAFS spectra; (e) magnetic layer hybrids and magnetization curves; (f) Raman spectrum; (g) NH_3-TPD curves; (h) Py-IR analysis; (i) water physisorption isotherms (inset: water contact angle).

X-ray photoelectron spectroscopy (XPS) was used to investigate the surface chemical composition of the catalyst as well as the valency states of the constituent elements. Figure 2b displays peaks at 779.9 and 781.1 eV, which are associated with metallic cobalt (Co^0) and bivalent cobalt (Co^{2+}).[37, 40] The concentration of Co species from XPS was determined to be 2.26 wt.% Co, comprising 1.52 wt.% Co^{2+} and 0.74 wt.% Co^0, which agreed with the ICP-OES and EDS results of 2.35 and 2.79 wt.% Co, respectively (Table S1). A sub band centered at 531.4 eV corresponding to surface-adsorbed oxygen species (O_A) was observed in Figure S3b, primarily pertaining to the oxygen-containing −OH functional groups produced through the HNO_3 etching process.[41] Additionally, the N 1s and C 1s spectra were

analyzed to explore the Co coordination environment. The obtained XPS spectra indicated that the pyridinic-N species in metal nitrides (Co–N_x moieties, 398.5 eV) and sp^2-bonded carbon in N- and O-containing aromatic rings (C–N–C and C–O–C, 285.5 eV), implying the formation of Co–N_x–C coordinate structural geometry.[42-44] These results were further confirmed by X-ray absorption near-edge structure (XANES) and extended X-ray absorption fine structure (EXAFS) spectroscopy. The Co near-edge position in Co–N–C was between that in Co foil and in CoO, as illustrated in Figure 2c, indicating that the average valence state of Co was intermediate between Co^0 and Co^{2+}. The linear combination fitting results revealed 27.9% Co^0 and 72.1% Co^{2+} in Figure 2d, which agreed with the XPS results. The peaks at 1.5 and 2.0 Å in the Co EXAFS spectrum can be assigned to metal–nitrogen (Co–N) and metal–metal (Co–Co) coordination, respectively.[45, 46] The EXAFS fitting results shown in Table S2 revealed that the Co–N coordination number is 3.8, which approaches 4, whereas the Co–Co coordination number was 6, confirming the existence of Co–N_4 and Co nanoclusters.[47] Therefore, the Co species in the Co–N–C NSs are composed of two bifunctional components: Co^{2+} species interacting indirectly with four N atoms and metal–metal coordinated Co^0. Typically, Co^{2+} (from Co–N_x moieties) in cooperation with −OH groups can serve as LASs and BASs and thus exhibit a primary catalytic role in CO_2 desorption, whereas Co^0 provide a magnetic aspect for the recovery of Co–N–C NSs. Given the large amounts of equipment needed, damage of catalyst and high running costs in conventional gravitational and centrifugal separation, magnetic catalysts can be easily separated and recovered from a heterogeneous system.[48] A magnetic separation experiment of Co–N–C NSs is shown in Figure 2e. The measured saturation magnetization of the Co–N–C NSs at room temperature was 20 emu·g^{-1}, which was sufficient for efficient magnetic separation.[49] As shown in the inset, Co–N–C NSs could be separated rapidly from the solution upon exposure to an external magnetic field.

The Raman spectrum of the Co–N–C catalyst, Figure 2f, had peaks located at 1578 cm^{-1} (G band) and 1357 cm^{-1} (D band). The I_D/I_G area ratio is 3.63 for the Co–N–C catalyst, indicating the amorphous nature of the Co–N–C and the presence of carbon defects arising from the high N and O doping.[50] Notably, these N or O atoms with lone pair of electrons might enable more polarity on the Co–N–C surface, thus

enhancing the hydrophilicity of SACs and assisting the MEA regeneration by inducing the proton H transfer *via* hydrogen bonding. Figure S4 shows the Fourier transform infrared (FTIR) spectra of the Co–N–C catalyst. The FTIR spectrum of the Co–N–C NSs exhibits three characteristic absorption bands at >3000 and 1200–1800 cm^{-1}, which were attributed to the stretching mode of the N–H bond, stretching modes of heterocycles, and the breathing mode of the benzene ring, respectively.[51] The amide I band at 1600 cm^{-1} and pyridine band at 1380 cm^{-1} suggest the formation of covalent bonds in the Co–N–C catalyst, resulting in good stability.[52]

The density and strength of the acid sites on the Co–N–C NSs were determined by ammonia temperature–programmed desorption analysis (NH_3-TPD) and the parameters are displayed in Figure 2g and Table S3. The desorption peaks at temperatures less than 300 °C were assigned to weak acid sites, and those in the range of 400−800 °C were assigned to strong acid sites.[21] The Co–N–C NSs exhibited desorption peaks at temperatures of 99 °C and 246 °C assigned to weak acid sites, with an acidity of 1.349 mmol/g. The presence of two desorption peaks at 467 °C and 670 °C, as well as a higher values of strong acid sites with 1.352 mmol/g, indicated that the Co–N–C NSs had a greater number of strong acid sites than previous catalysts.[25] The pyridine-adsorption infrared (Py-IR) technique was used as a qualitative probe to distinguish the acid site types (BASs and LASs) in the Co–N–C NSs catalyst (Figure 2h and Table S3). The typical characteristic of BASs was observed at 1492 and 1545 cm^{-1} and that of LAS at 1444, 1492 and 1604 cm^{-1} in the Py-IR spectrum, indicating the existence of unsaturated metal ions exposed on the surface of the catalysts and available H-bond donor sites from the surface –OH groups.[30] The numerous BASs and LASs as well as the B/L ratio (0.12) of Co–N–C NSs were caused primarily by the introduction of a high number of –OH groups (BASs) *via* the HNO_3 etching procedure, and the accessible and abundant active Co–N_x (LASs). BASs and LASs associated with enhanced proton and electron transport are anticipated to contribute to higher catalytic efficiency and CO_2 desorption.

In addition, Figure 2i shows the low-pressure water physisorption isotherms of the prepared Co–N–C catalysts. Together with the N_2 adsorption–desorption isotherm results in Figure S5, the high specific surface area (108.5 $m^2 \cdot g^{-1}$), high uptake (9.3 $mmol \cdot g^{-1}$) of H_2O at 25 °C and pore volume (0.106 cm^3/g)

over the Co–N–C NSs confirmed their unusual hydrophilic nature and the existence of rich microporosity.[34] As shown in the inset, contact angles of 15.8° and 17.2° were observed on the Co–N–C NSs at low pressures, which outperforms the widely used commercial carbon catalysts of 138° and 137°. The superhydrophilic surface of the Co–N–C NSs catalyst can be ascribed to the large number of hydrogen bonding =N- and O-doped active sites, which enables their highly efficient accessibility with polar guests $RNHCOO^-$, RNH_3^+ and H_3O^+, and results in the promotion of proton transfer and subsequent CO_2 desorption.[53]

3.2 Catalytic performance of Co–N–C NSs

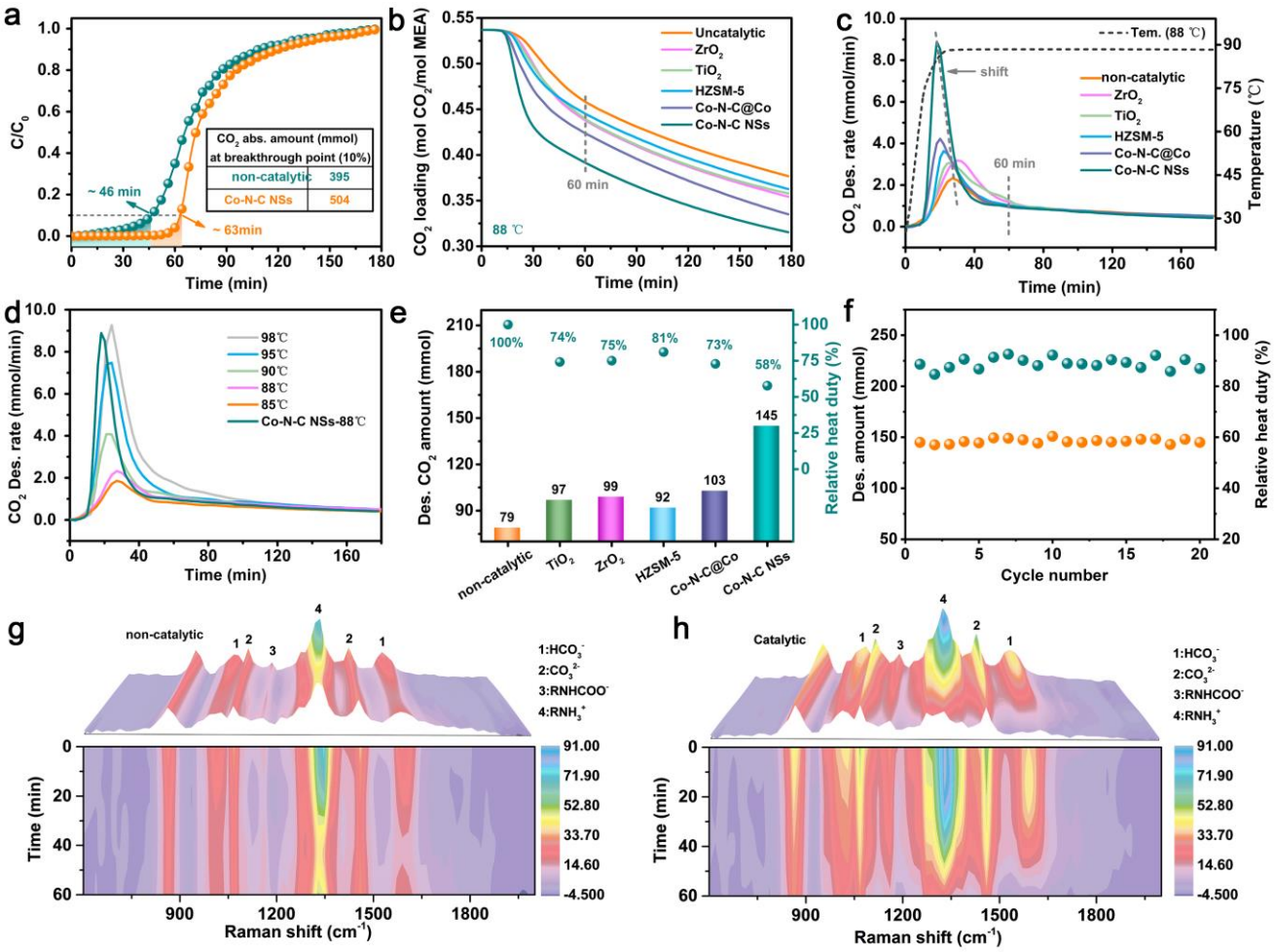

Figure 3. Catalytic properties of as-prepared catalysts in 5 M MEA solution: (a) CO_2 absorption curves with Co–N–C NSs; (b) CO_2 loading change curves at 88 °C; (c) CO_2 desorption (des.) rate; (d) CO_2 desorption (des.) rate compared with non-catalytic property in different temperature; (e) amount of desorbed (Des.) CO_2 and relative heat duty; (f) recyclability test results for Co–N–C NSs (des. CO_2

amount was recorded at 180 min); (g and h) Raman spectra of solutions at different times during the CO_2 desorption experiments without and with catalyst.

The catalytic activity of the as-prepared samples on CO_2 absorption and desorption for the 5 M (mol/L) MEA solution was evaluated in terms of CO_2 loading as well as the amount and rate of CO_2 desorption in Figure 3. In general, BASs and LASs can serve as proton donors and acceptors to facilitate the formation of RNH_3^+ and $RNHCOO^-$ during the CO_2 absorption process. Furthermore, because of the increased collision disturbance between particles and the gas–liquid barrier, CO_2 mass transfer resistance can be diminished.[54, 55] Thus, Co–N–C NSs equipped with strong acidity and 2D structure could significantly alter the CO_2 absorption breakthrough curves. Figure 3a shows the catalytic CO_2 absorption with and without Co–N–C NSs for 5M MEA solution with a gas mixture of 50 vol.% CO_2 and 50 vol.% N_2 at a flow rate of 400 mL·min^{-1}. The breakthrough value was defined as absorbed CO_2 amount at a time that the CO_2 concentration in the reactor outlet was 10% of the feed concentration. The breakthrough time without catalyst was 46 min, which was consistent with that of ~43 min observed by Lai.[13] While, Co–N–C NSs increase the breakthrough time to 63 min, approximately 37% improvement compared with the non-catalytic absorption. Accordingly, the absorbed CO_2 amount at breakthrough also increased from 395 mmol to 504 mmol, suggesting that the CO_2 absorption efficiency was increased 28% by adding Co–N–C NSs.

Excellent CO_2 desorption is crucial in CCS technology due to energy economy.[13] The CO_2 desorption performance of the various catalysts was evaluated by heating 5 M CO_2-rich MEA solution with initial CO_2 loading at 0.53±0.01 mol of CO_2/mol amine at 88 °C. An optimal concentration of the catalysts was set as 0.1 wt.% for Co–N–C @Co and Co–N–C NSs and 1 wt.% for recently reported ZrO_2, TiO_2 and HZSM-5 (Figure S6b). Figures 3b-c indicates an enhancement of the CO_2 desorption kinetics using the above catalysts. The Co–N–C NSs catalyst exhibited the best catalytic activity among all the catalysts, much better than ZrO_2, TiO_2, HZSM-5 and Co–N–C@Co. The most favorable catalytic CO_2 desorption rate of 8.9 mmol/min of Co–N–C NSs was 281% higher than the non-catalytic process at 88 °C. After the CO_2 sorption reached breakthrough, the component change of the CO_2-loaded MEA solution in the CO_2

desorption process during the first 60 min was further monitored by Raman spectroscopy as shown in Figure 3g-h. The higher peak intensity of RNH_2^+ and $RNHCOO^-$ at the initial time confirmed that Co–N–C NSs were favorable to increase the CO_2 absorption efficiency. The typically peak intensities of HCO_3^-, CO_3^{2-}, RNH_2^+ and $RNHCOO^-$ during catalytic CO_2 desorption noticeably decreased, suggesting that the addition of Co–N–C NSs was beneficial to the MEA regeneration and thus quickly enhanced the reaction kinetics.[56, 57] Additionally, the temperature corresponding to the highest desorption rate shifted to lower values in Figure 3c, implying that a new catalytic path with low activation energy was obtained for carbamate breakdown. As shown in Figure 3d, the Co–N–C NSs catalyst exhibited similar CO_2 desorption rate compared with the non-catalytic one of approximately 9.3 mmol/min at 98 °C. Thus, the addition of Co–N–C NSs catalyst enabled a decrease of CO_2 desorption temperatures reduced by 10 °C. It is worth noting that the expensive CO_2 desorption step in conventional CO_2 capture technologies that operate at higher temperatures is primarily caused by the high specific and latent heat capacities of water.[13, 19] As a control, Figure S7a investigates the volatilization of amine solution at different temperatures. The results indicated that the volatile liquid substantially decreased by 20.3% when the temperature decreased from 98 °C to 88 °C. From Table S4, the 20.3% decrease of volatile liquid from 98 °C to 88 °C enabled a substantial reduction in the heat duty of approximately 71.7% for CO_2 capture. Moreover, ^{13}C NMR was used to investigate the components of the volatile liquid at 88 °C and 98 °C (Figure S7b). From the spectra of fresh 5M MEA and CO_2-rich MEA, negligible peaks were observed in the spectra indicated that the volatile liquid at 88 °C was mainly composed of water, while insignificant amine peaks were detected in volatile liquid at 98 °C.[58] Consequently, the decreased desorption temperature at 88 °C using efficient Co–N–C NSs catalyst could decrease the evaporation energy consumption and suppress MEA degradation at high temperatures.

Figure 3e compares the relative heat duty percentages as well as the CO_2 desorption amount of the various catalysts. Because the desorption rate after 60 minutes was similar in Figure 3c, the desorbed CO_2 quantity at 60 minutes was used as a reference. Together with the results presented in Table S4, Co–N–C NSs exhibited the best catalytic activity, with an approximate 83.5% increase in the CO_2 desorption

amount, and 42% decrease in heat duty when compared to the reaction without catalysts at 88 °C; and 71.7% decrease in heat duty when compared to the reaction without catalysts at 98 °C. As shown in Figure S8, although the concentration of Co–N–C NSs was 0.1wt.% and only 5~10% of previous SACs, Co–N–C NSs achieved the most improved catalytic activity, which was a ~10-fold enhancement in efficiency compared with the solid acid catalysts from previous heterogeneous catalysts. Moreover, Figure S9 and Table S5 indicated an improvement in efficiency and energy of typical amine (including: diethanolamine, methyldiethanolamine and their combination) under Co–N–C NSs catalysis, further identifying the better versatility of this catalyst. In addition, the recycling stability of Co–N–C NSs was determined using 20 cycles of absorption–desorption. As shown in Figure 3f and S10, negligible or no decrease in catalytic performances were observed after 20 cycles within 3600 min, including CO_2 desorption amounts, CO_2 desorption rate, desorbed CO_2 amount and regenerative energy. The 20th recycled Co–N–C NSs catalyst was characterized through ICP, XPS, and HRTEM (Figure S11 and Table S6). The results indicated negligible leaching of Co^{2+} at 0.0012 wt% and good structural integrity after multiple regenerations, indicating the excellent stability of Co–N–C NSs at high regeneration temperatures. To confirm the high stability of Co^{2+} species, the contact interface between Co and N_x (x=1, 2, 3, 4) was calculated based on DFT calculations. As suggested by Figure S12, the Co^{2+} cohesive energy (E_c) increased with increased coordinated N atoms, suggesting that the generation of Co–N_4 species in the Co–C–N NSs is beneficial for its stability and might help restrict the aggregation between Co species with –NH_2 groups, thus stopping the active Co^{2+} components stripping away from the surface of catalyst.[59]

3.3 Theoretical MEA regeneration mechanism

The catalytic performance with Co^0 and Co^{2+} ions in CO_2-riched MEA solvents was evaluated by combining the density functional theory (DFT) calculation of the carbamate decomposition on Co^0 nanoclusters and Co-N_4 active sites (Figure S6a and S15). The results indicated that the presence of Co^{2+} instead of Co^0 species of Co–N–C NSs accounted for a significant acceleration of MEA regeneration. In order to determine the enhanced carbamate decomposition catalyzed by Co–N_4 and –OH acid sites of Co–N–C NSs at an atomic level, DFT calculations were employed in Figure 4 and S14. According to the

traditional zwitterion mechanism in Eqs 1-2, the rich MEA solution regeneration process without catalysts involves two steps, including the N–C rupture of carbamate ($RNHCOO^-$) by reacting with H_3O^+ and amine-H^+ (RNH_3^+) deprotonation after reacting with H_2O. The non-catalytic reaction pathways were investigated and detailed in Figure 4a. The O atom of $RNHCOO^-$ first reacts with protonated H_3O^+. An isomerization process where proton hydrogen transfers from O to the N atom occurs, leading to the acceleration of N–C rapture and generation of CO_2 molecules. H_2O serves as proton receptors and react with proton carrying species RNH_3^+ and form MEA (RNH_2) and H_3O^+. These results indicate that proton transfer between $RNHCOO^-$ and H_3O^+ or $MEAH^+$ and H_2O is the rate–determining step with high energy barriers (1.46 and 1.09 eV, respectively). The restricted proton transfer in alkaline solutions results in a high energy input for the decomposition of $RNHCOO^-$ to CO_2.

$$\mathrm{RNHCOO^- + H_3O^+ \leftrightarrow Zwitterion \leftrightarrow RNH_2 + CO_2 + H_2O} \tag{1}$$

$$\mathrm{RNH_3^+ + H_2O/HCO_3^- \leftrightarrow RNH_2 + H_3O^+/H_2CO_3} \tag{2}$$

Based on results obtained from this study, Co-N_4 LASs and –OH BASs could be used as active sites to synergistically facilitate the CO_2 desorption rate and decrease the energy penalty. The electronic properties of the $RNHCOO^-$ were first calculated to investigate the potential reaction mechanism. As shown in Figure S14a, the negative Bader charge value of N (-1.12 e) and O (-0.97 e) indicates the nucleophilicity of N and O atoms of $RNHCOO^-$. Considering the electrophilicity of the Co species of Co–N_4 LASs, it could be assumed that the reactions between $RNHCOO^-$ with Co–N_4 LASs are involved in two pathways, corresponding to interaction by the N–Co bond (path I) or the O–Co bond (path II). The optimized absorption structures in Figure S14-c indicated that the lengths of the N–C bond of $RNHCOO^-$ connected with the Co atom by the N–Co bond increased slightly, whereas when connected by the O–Co bond they decreased. These results suggest that the chemically reactive N–Co intermediate between $RNHCOO^-$ and Co–N–C NSs can weaken the covalent interaction of the N–C bond and thus plays an essential part in the N–C bond rapture and CO_2 desorption. The charge difference density of $RNHCOO^-$ connected with the Co atom of Co–N–C NSs in Figure S16 further indicates a decreased charge density around the nucleophilic N of $RNHCOO^-$, while an increase around the oxycarbide is observed. The

weakened charge density between N and C atoms indicates a reduction of energy required to break the N–C bond.

To further understand the extraordinary MEA regeneration activity of Co–N–C NSs, the aforementioned two reaction pathways of $RNHCOO^-$ decomposition on Co–N_x and –OH sites are detailed in Figure 4b and 4c. Typically, for catalytic path I in Figure 4b, $RNHCOO^-$ is first adsorbed on the catalytic surface, and its N atom is then directly attacked by Co–N_x sites and its O atom is connected with proton bearing species –OH sites, resulting in a decrease of charge density between N and C atoms and subsequent increase of N–C bonds. Afterward, an isomerization process where proton hydrogen transfers from O to the N atom occurs, leads to the further acceleration of N–C rapture and generation of CO_2 molecules. Then, the formed MEA (RNH_2) molecule desorbs from the surface and the residual proton-deficient O sites further react with proton containing species RNH_3^+. The overall reactions are given in Eqs 3-4. Compared with the non-catalytic process in Figure 4a, –OH BASs instead of H_3O^+ served as proton donors and proton-deficient O sites instead of H_2O serve as proton receptors in this catalytic process. The rate-determining steps in Figure 4b are the proton transfer and RNH_2 molecule desorption, which require an energy barrier of 1.32 and 0.41 eV, respectively. However, for the MEA regeneration in catalytic path II, the main difference from the catalytic path I was the adsorption of $RNHCOO^-$ to the catalyst surface. The adsorbed $RNHCOO^-$ resulted in a higher energy barrier (2.58 eV) when its N atom is attacked by protons to generate CO_2 molecules. Consequently, the resistance of MEA regeneration in catalytic path I is lower than that of non-catalytic processes at 0.14 eV, which explains the excellent performance of solid acid catalysts and implies that the energy required for CO_2 desorption can be substantially decreased. The catalytic N–C bond rupture and proton-donating ability of the catalysts are the major factors influencing the energy requirement for the decomposition of $RNHCOO^-$ to CO_2. The easily accessible Co-N_4 LASs on the catalyst surfaces serves as accelerants for N–C bond rupture, whereas the abundant –OH BASs served as proton donors, thereby accelerating the transformation of $RNHCOO^-$ into MEA and CO_2 thereby reducing the energy required for CO_2 capture.

$$\mathrm{RNHCOO^- + H\_Cat. \leftrightarrow Zwitterion \leftrightarrow RNH_2 + CO_2 + *\_Cat.} \quad (3)$$

$$RNH_3^+ + *\_Cat. \leftrightarrow RNH_2 + H\_Cat. \quad (4)$$

H-Cat. and *-Cat. denote the BASs and proton-deficient conjugate base sites on the Co–N–C NSs, respectively.

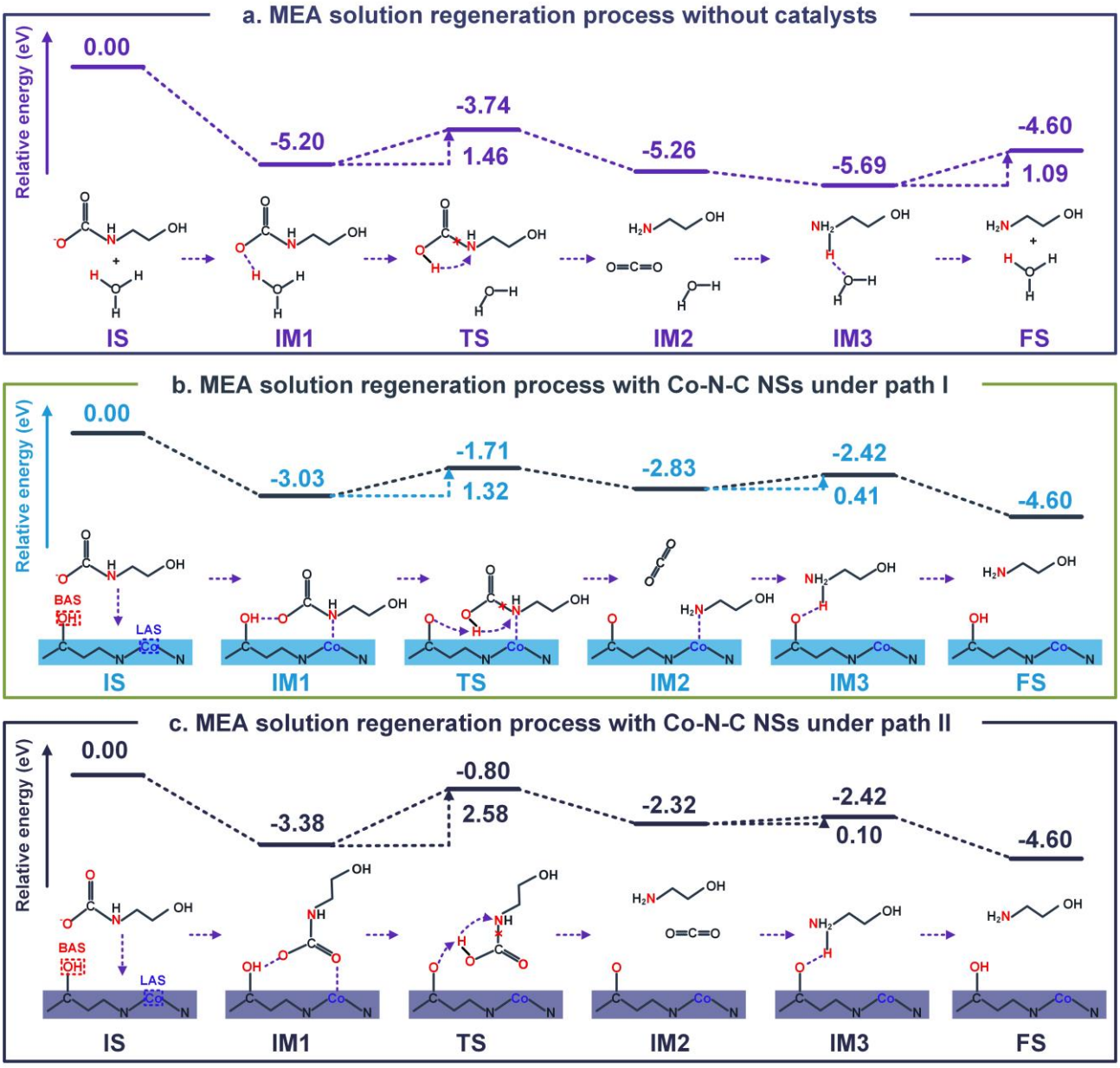

Figure 4. Relative energy and mechanism of action of the various species along the reaction pathway of MEA regeneration: (a) non-catalytic process, catalytic reaction with Co–N–C NSs under (b) path I and (c) path II.

3.4 Environmental Implications

CO_2 capture and storage (CCS) technique *via* amine-based chemisorption using MEA absorbents by the formation of C–N bond holds the key to address global warming and climate change. This amine

scrubbing method has become the most cost-effective method for CCS, since it is possible to scale up the approach for real-world scenarios to treat tons of CO_2-containing gases. For example, engineering, construction, and service companies or leaders in power generation are significantly invested in this technology, which can be envisioned as a retrofit or add-on to existing power plants. The investigated Co–N–C NSs can lower regeneration temperature to minimize indirect CO_2 emissions due to the usage of fuels to reach the required temperature, hence enables power plants to achieve net zero carbon emissions. In summary, our study provides an energy-efficient CO_2 capture pathway as well as a detailed understanding of the catalytic process, which can be used to provide predictive guidelines for the development of new nanomaterials, particularly metal-containing 2D MOF-mediated carbon structures, for MEA regeneration in CCS, and for other electrocatalytic and photocatalytic reactions.

Associated content

Supporting Information. Illustration of catalyst synthesis strategy and characterization. Relative CO_2 desorption/absorption experiment and results. Details for DFT simulation.

Acknowledgements

This research is supported by the National Natural Science Foundation of China (No. 21706061, No. 21876157, No. 22176057, and No. 22276051), China Postdoctoral Science Foundation (2022TQ0175) and the Central Government Guided Local Science and Technology Development Fund (No. 2021ZY1022 and XM2112344).

Reference

(1). Meys, R.; Kätelhön, A.; Bachmann, M.; Winte, B.; Zibunas, C.; Suh, S.; Bardow, A., Achieving net-zero greenhouse gas emission plastics by a circular carbon economy. *Science* **2021,** *374*, 6563.

(2). Ou, Y.; Iyer, G.; Clarke, L.; Edmonds, J.; Fawcett, A. A.; Hultman, N.; McFarland, J. R.; Binsted, M.; Cui, R.; Fyson, C.; Geiges, A.; Gonzales-Zuñiga, S.; Gidden, M. J.; Höhne, N.; Jeffery, L.; Kuramochi, T.; Lewis, J.; Meinshausen, M.; Nicholls, Z.; Patel, P.; Ragnauth, S.; Rogelj, J.; Waldhoff, S.; Yu, S.; McJeon, H., Can updated climate pledges limit warming well below 2°C? *Science* **2021,** *374*, (6568), 690-693.

(3). Hoegh-Guldberg, O.; Jacob, D.; Taylor, M.; Guillen Bolanos, T.; Bindi, M.; Brown, S.; Camilloni, I. A.; Diedhiou, A.; Djalante, R.; Ebi, K.; Engelbrecht, F.; Guiot, J.; Hijioka, Y.; Mehrotra, S.; Hope, C. W.; Payne, A. J.; Portner, H. O.; Seneviratne, S. I.; Thomas, A.; Warren, R.; Zhou, G., The human imperative of stabilizing global climate change at 1.5 °C. *Science* **2019,** *365*, (6459), eaaw6974

(4). Bednar, J.; Obersteiner, M.; Baklanov, A.; Thomson, M.; Wagner, F.; Geden, O.; Allen, M.; Hall, J. W., Operationalizing the net-negative carbon economy. *Nature* **2021,** *596*, (7872), 377-383.

(5). Verheggen, B.; Strengers, B.; Cook, J.; van Dorland, R.; Vringer, K.; Peters, J.; Visser, H.; Meyer, L., Scientists' views about attribution of global warming. *Environ. Sci. Technol.* **2014,** *48*, (16), 8963-8971.

(6). Hu, Z.; Wang, Y.; Shah, B. B.; Zhao, D., CO_2 Capture in Metal-Organic Framework Adsorbents: An Engineering Perspective. *Adv. Sustain. Syst.* **2019,** *3*, (1), 1800080.

(7). Lv, B.; Guo, B.; Zhou, Z.; Jing, G., Mechanisms of CO_2 Capture into Monoethanolamine Solution with Different CO_2 Loading during the Absorption/Desorption Processes. *Environ. Sci. Technol.* **2015,** *49*, (17), 10728-10735.

(8). Liu, H.; Jiang, X.; Idem, R.; Dong, S.; Tontiwachwuthikul, P., AI models for correlation of physical properties in system of 1DMA2P-CO_2-H_2O. *AIChE J.* **2022,** *68*, (9), e17761.

(9). Rochelle, G. T., Amine scrubbing for CO_2 capture. *Science* **2009,** *325*, 5948.

(10). Bae, Y. S.; Snurr, R. Q., Development and evaluation of porous materials for carbon dioxide separation and capture. *Angew. Chem. Int. Ed.* **2011,** *50*, (49), 11586-11596.

(11). Bui, M.; Adjiman, C. S.; Bardow, A.; Anthony, E. J.; Boston, A.; Brown, S.; Fennell, P. S.; Fuss, S.; Galindo, A.; Hackett, L. A.; Hallett, J. P.; Herzog, H. J.; Jackson, G.; Kemper, J.; Krevor, S.; Maitland, G. C.; Matuszewski, M.; Metcalfe, I. S.; Petit, C.; Puxty, G.; Reimer, J.; Reiner, D. M.; Rubin, E. S.; Scott, S. A.; Shah, N.; Smit, B.; Trusler, J. P. M.; Webley, P.; Wilcox, J.; Mac Dowell, N., Carbon capture and storage (CCS): the way forward. *Energy Environ. Sci.* **2018,** *11*, (5), 1062-1176.

(12). Siegelman, R. L.; Kim, E. J.; Long, J. R., Porous materials for carbon dioxide separations. *Nat. Mater.* **2021,** *20*, (8), 1060-1072.

(13). Lai, Q.; Toan, S.; Assiri, M. A.; Cheng, H.; Russell, A. G.; Adidharma, H.; Radosz, M.; Fan, M., Catalyst-$TiO(OH)_2$ could drastically reduce the energy consumption of CO_2 capture. *Nat. Commun.* **2018,** *9*, (1), 2672.

(14). Alivand, M. S.; Mazaheri, O.; Wu, Y.; Stevens, G. W.; Scholes, C. A.; Mumford, K. A., Catalytic Solvent Regeneration for Energy-Efficient CO_2 Capture. *ACS Sustain.Chem. Eng.* **2020,** *8*, (51), 18755-18788.

(15). Gao, H.; Huang, Y.; Zhang, X.; Bairq, Z. A. S.; Huang, Y.; Tontiwachwuthikul, P.; Liang, Z., Catalytic performance and mechanism of SO_4^{2-}/ZrO_2/SBA-15 catalyst for CO_2 desorption in CO_2-loaded monoethanolamine solution. *Appl. Energy* **2020,** *259*, 114179.

(16). Xing, L.; Wei, K.; Li, Q.; Wang, R.; Zhang, S.; Wang, L., One-Step Synthesized SO_4^{2-}/ZrO_2-HZSM-5 Solid Acid Catalyst for Carbamate Decomposition in CO_2 Capture. *Environ. Sci. Technol.* **2020,** *54*, (21), 13944-13952.

(17). Bhatti, U. H.; Shah, A. K.; Hussain, A.; Khan, H. A.; Park, C. Y.; Nam, S. C.; Baek, I. H., Catalytic activity of facilely synthesized mesoporous HZSM-5 catalysts for optimizing the CO_2 desorption rate from CO_2-rich amine solutions. *Chem. Eng. J.* **2020,** *389*, 123439.

(18). Zhang, X.; Zhang, X.; Liu, H.; Li, W.; Xiao, M.; Gao, H.; Liang, Z., Reduction of energy requirement of CO_2 desorption from a rich CO_2-loaded MEA solution by using solid acid catalysts. *Appl. Energy* **2017,** *202*, 673-684.

(19). Bhatti, U. H.; Kazmi, W. W.; Min, G. H.; Haider, J.; Nam, S.; Baek, I. H., Facilely Synthesized M-Montmorillonite (M = Cr, Fe, and Co) as Efficient Catalysts for Enhancing CO_2 Desorption from Amine Solution. *Ind. Eng. Chem. Res.* **2021,** *60*, (36), 13318-13325.

(20). Ali Saleh Bairq, Z.; Gao, H.; Huang, Y.; Zhang, H.; Liang, Z., Enhancing CO_2 desorption performance in rich MEA solution by addition of $SO_4^{2-}/ZrO_2/SiO_2$ bifunctional catalyst. *Appl. Energy* **2019,** *252*, 113440.

(21). Bairq, Z. A. S.; Gao, H.; Murshed, F. A. M.; Tontiwachwuthikul, P.; Liang, Z., Modified Heterogeneous Catalyst-Aided Regeneration of CO_2 Capture Amines: A Promising Perspective for a Drastic Reduction in Energy Consumption. *ACS Sustain.Chem. Eng.* **2020,** *8*, (25), 9526-9536.

(22). Xing, L.; Wei, K.; Li, Y.; Fang, Z.; Li, Q.; Qi, T.; An, S.; Zhang, S.; Wang, L., TiO_2 Coating Strategy for Robust Catalysis of the Metal-Organic Framework toward Energy-Efficient CO_2 Capture. *Environ. Sci. Technol.* **2021,** *55*, (16), 11216-11224.

(23). Liu, H.; Jiang, X.; Idem, R.; Dong, S.; Tontiwachwuthikul, P., Comprehensive reaction kinetics model of CO_2 absorption into 1-dimethylamino-2-propanol solution. *AIChE J.* **2022,** *68*, (11), e17816.

(24). Moioli, S.; Ho, M. T.; Wiley, D. E.; Pellegrini, L. A., Assessment of carbon dioxide capture by precipitating potassium taurate solvent. *Int. J. Green. Gas Con.* **2019,** *87*, 159-169.

(25). Liu, S.; Zhu, M.; Iqbal, M., Research Progress on Stability of Solid Acid Catalysts. *Catal. Surv. Asia* **2020,** *24*, (3), 196-206.

(26). Zhang, X.; Zhu, Z.; Sun, X.; Yang, J.; Gao, H.; Huang, Y.; Luo, X.; Liang, Z.; Tontiwachwuthikul, P., Reducing Energy Penalty of CO_2 Capture Using Fe Promoted SO_4^{2-}/ZrO_2/MCM-41 Catalyst. *Environ. Sci. Technol.* **2019,** *53*, (10), 6094-6102.

(27). Sun, Q.; Li, T.; Mao, Y.; Gao, H.; Sema, T.; Wang, S.; Liu, L.; Liang, Z., Reducing Heat Duty of MEA Regeneration Using a Sulfonic Acid-Functionalized Mesoporous MCM-41 Catalyst. *Ind. Eng. Chem. Res.* **2021,** *60*, (50), 18304-18315.

(28). Xing, L.; Li, M.; Qi, T.; Mao, L.; Hu, Z.; Zhang, E.; Hao, G. P.; Mao, B.; Wang, L., Construction of Confined Bifunctional 2D Material for Efficient Sulfur Resource Recovery and Hg^{2+} Adsorption in Desulfurization. *Environ. Sci. Technol.* **2022,** *56*, (7), 4531-4541.

(29). Rui, K.; Zhao, G.; Chen, Y.; Lin, Y.; Zhou, Q.; Chen, J.; Zhu, J.; Sun, W.; Huang, W.; Dou, S. X., Hybrid 2D Dual-Metal–Organic Frameworks for Enhanced Water Oxidation Catalysis. *Adv. Funct. Mater.* **2018,** *28*, (26), 1801554.

(30). Hao, G.-P.; Jin, Z.-Y.; Sun, Q.; Zhang, X.-Q.; Zhang, J.-T.; Lu, A.-H., Porous carbon nanosheets with precisely tunable thickness and selective CO_2 adsorption properties. *Energy Environ. Sci.* **2013,** *6*, (12), 3740.

(31). Ye, Y.; Li, H.; Cai, F.; Yan, C.; Si, R.; Miao, S.; Li, Y.; Wang, G.; Bao, X., Two-Dimensional Mesoporous Carbon Doped with Fe–N Active Sites for Efficient Oxygen Reduction. *ACS Catal.* **2017,** *7*, (11), 7638-7646.

(32). Ang, H.; Hong, L., Polycationic Polymer-Regulated Assembling of 2D MOF Nanosheets for High-Performance Nanofiltration. *ACS Appl Mater Interfaces* **2017,** *9*, (33), 28079-28088.

(33). Coleman, J. N.; Lotya, M.; O'Neill, A.; Bergin, S. D.; King, P. J., Two-dimensional nanosheets produced by liquid exfoliation of layered materials. *Science* **2011,** *331*, 6017.

(34). Hao, G. P.; Tang, C.; Zhang, E.; Zhai, P.; Yin, J.; Zhu, W.; Zhang, Q.; Kaskel, S., Thermal Exfoliation of Layered Metal-Organic Frameworks into Ultrahydrophilic Graphene Stacks and Their Applications in Li-S Batteries. *Adv. Mater.* **2017,** *29*, (37), 1702829.

(35). Tu, S.; Ming, F.; Zhang, J.; Zhang, X.; Alshareef, H. N., MXene-Derived Ferroelectric Crystals. *Adv. Mater.* **2019,** *31*, (14), 1806860.

(36). Zhao, J.; Wang, J.; Bi, R.; Yang, M.; Wan, J.; Jiang, H.; Gu, L.; Wang, D., General Synthesis of Multiple-Cores@Multiple-Shells Hollow Composites and Their Application to Lithium-Ion Batteries. *Angew. Chem. Int. Ed.* **2021,** *60*, (49), 25719-25722.

(37). Pei, Y.-P.; Liu, J.-X.; Zhao, Y.-H.; Ding, Y.-J.; Liu, T.; Dong, W.-D.; Zhu, H.-J.; Su, H.-Y.; Yan, L.; Li, J.-L.; Li, W.-X., High Alcohols Synthesis via Fischer–Tropsch Reaction at Cobalt Metal/Carbide Interface. *ACS Catal.* **2015,** *5*, (6), 3620-3624.

(38). Liu, Y. T.; Zhang, P.; Sun, N.; Anasori, B.; Zhu, Q. Z.; Liu, H.; Gogotsi, Y.; Xu, B., Self-Assembly of Transition Metal Oxide Nanostructures on MXene Nanosheets for Fast and Stable Lithium Storage. *Adv. Mater.* **2018,** *30*, (23), 1707334.

(39). Liu, X.; Liu, W.; Ko, M.; Park, M.; Kim, M. G.; Oh, P.; Chae, S.; Park, S.; Casimir, A.; Wu, G.; Cho, J., Metal (Ni, Co)-Metal Oxides/Graphene Nanocomposites as Multifunctional Electrocatalysts. *Adv. Funct. Mater.* **2015,** *25*, (36), 5799-5808.

(40). Wang, L.; Zhang, W.; Zheng, X.; Chen, Y.; Wu, W.; Qiu, J.; Zhao, X.; Zhao, X.; Dai, Y.; Zeng, J., Incorporating nitrogen atoms into cobalt nanosheets as a strategy to boost catalytic activity toward CO_2 hydrogenation. *Nat. Energy* **2017,** *2*, (11), 869-876.

(41). Chen, D.; He, D.; Lu, J.; Zhong, L.; Liu, F.; Liu, J.; Yu, J.; Wan, G.; He, S.; Luo, Y., Investigation of the role of surface lattice oxygen and bulk lattice oxygen migration of cerium-based oxygen carriers: XPS and designed H2-TPR characterization. *Appl. Catal. B* **2017,** *218*, 249-259.

(42). Guo, F.; Yang, P.; Pan, Z.; Cao, X. N.; Xie, Z.; Wang, X., Carbon-Doped BN Nanosheets for the Oxidative Dehydrogenation of Ethylbenzene. *Angew. Chem. Int. Ed.* **2017,** *56*, (28), 8231-8235.

(43). Zhou, H.; Yang, T.; Kou, Z.; Shen, L.; Zhao, Y.; Wang, Z.; Wang, X.; Yang, Z.; Du, J.; Xu, J.; Chen, M.; Tian, L.; Guo, W.; Wang, Q.; Lv, H.; Chen, W.; Hong, X.; Luo, J.; He, D.; Wu, Y., Negative Pressure Pyrolysis Induced Highly Accessible Single Sites Dispersed on 3D Graphene Frameworks for Enhanced Oxygen Reduction. *Angew. Chem. Int. Ed.* **2020,** *59*, (46), 20465-20469.

(44). Xie, X.; Chen, C.; Zhang, N.; Tang, Z.-R.; Jiang, J.; Xu, Y.-J., Microstructure and surface control of MXene films for water purification. *Nat. Sustain.* **2019,** *2*, (9), 856-862.

(45). Kuznetsov, D. A.; Chen, Z.; Kumar, P. V.; Tsoukalou, A.; Kierzkowska, A.; Abdala, P. M.; Safonova, O. V.; Fedorov, A.; Muller, C. R., Single Site Cobalt Substitution in 2D Molybdenum Carbide (MXene) Enhances Catalytic Activity in the Hydrogen Evolution Reaction. *J. Am. Chem. Soc.* **2019,** *141*, (44), 17809-17816.

(46). Zhao, J.; Peng, Q.; Wang, Z.; Xu, W.; Xiao, H.; Wu, Q.; Sun, H. L.; Ma, F.; Zhao, J.; Sun, C. J.; Zhao, J.; Li, J., Proton mediated spin state transition of cobalt heme analogs. *Nat. Commun.* **2019,** *10*, (1), 2303.

(47). Zhu, W.; Zhang, L.; Liu, S.; Li, A.; Yuan, X.; Hu, C.; Zhang, G.; Deng, W.; Zang, K.; Luo, J.; Zhu, Y.; Gu, M.; Zhao, Z. J.; Gong, J., Enhanced CO2 Electroreduction on Neighboring Zn/Co Monomers by Electronic Effect. *Angew. Chem. Int. Ed.* **2020,** *59*, (31), 12664-12668.

(48). Xia, J.; Mahandra, H.; Ghahreman, A., Efficient Gold Recovery from Cyanide Solution Using Magnetic Activated Carbon. *ACS Appl. Mater. Interfaces* **2021,** *13*, (40), 47642-47649.

(49). Wang, J.; Zhang, Q.; Deng, F.; Luo, X.; Dionysiou, D. D., Rapid toxicity elimination of organic pollutants by the photocatalysis of environment-friendly and magnetically recoverable step-scheme $SnFe_2O_4/ZnFe_2O_4$ nano-heterojunctions. *Chem. Eng. J.* **2020,** *379*, 122264.

(50). Ju, W.; Bagger, A.; Hao, G. P.; Varela, A. S.; Sinev, I.; Bon, V.; Roldan Cuenya, B.; Kaskel, S.; Rossmeisl, J.; Strasser, P., Understanding activity and selectivity of metal-nitrogen-doped carbon catalysts for electrochemical reduction of CO2. *Nat. Commun.* **2017,** *8*, (1), 944.

(51). Zhang, S.; Jiang, S.-F.; Huang, B.-C.; Shen, X.-C.; Chen, W.-J.; Zhou, T.-P.; Cheng, H.-Y.; Cheng, B.-H.; Wu, C.-Z.; Li, W.-W.; Jiang, H.; Yu, H.-Q., Sustainable production of value-added carbon nanomaterials from biomass pyrolysis. *Nat. Sustain.* **2020,** *3*, (9), 753-760.

(52). Zhou, T.; Du, Y.; Yin, S.; Tian, X.; Yang, H.; Wang, X.; Liu, B.; Zheng, H.; Qiao, S.; Xu, R., Nitrogen-doped cobalt phosphate@nanocarbon hybrids for efficient electrocatalytic oxygen reduction. *Energy Environ. Sci.* **2016,** *9*, (8), 2563-2570.

(53). Akizuki, M.; Oshima, Y., Solid Acid/Base Catalysis in Sub- and Supercritical Water. *Ind. Eng. Chem. Res.* **2018,** *57*, (16), 5495-5506.

(54). Cheng, S.-Y.; Liu, Y.-Z.; Qi, G.-S., Experimental study of CO_2 capture enhanced by coal fly ash-synthesized NH_2-MCM-41 coupled with high gravity technology. *Chem. Eng. J.* **2020,** *400*, 125946.

(55). Quan, H.; Dong, S.; Zhao, D.; Li, H.; Geng, J.; Liu, H., Generic AI models for mass transfer coefficient prediction in amine-based CO_2 absorber, Part II: RBFNN and RF model. *AIChE J. n/a*, e17904.

(56). Wong, M. K.; Bustam, M. A.; Shariff, A. M., Chemical speciation of CO_2 absorption in aqueous monoethanolamine investigated by in situ Raman spectroscopy. *Int. J. Greenh. Gas Con.* **2015,** *39*, 139-147.

(57). Alivand, M. S.; Mazaheri, O.; Wu, Y.; Zavabeti, A.; Christofferson, A. J.; Meftahi, N.; Russo, S. P.; Stevens, G. W.; Scholes, C. A.; Mumford, K. A., Engineered assembly of water-dispersible nanocatalysts enables low-cost and green CO_2 capture. *Nat. Commun.* **2022,** *13*, (1), 1249.

(58). Wang, L.; Zhang, Y.; Wang, R.; Li, Q.; Zhang, S.; Li, M.; Liu, J.; Chen, B., Advanced Monoethanolamine Absorption Using Sulfolane as a Phase Splitter for CO_2 Capture. *Environ. Sci. Technol.* **2018,** *52*, (24), 14556-14563.

(59). Li, J.; Cui, W.; Sun, Y.; Chu, Y.; Cen, W.; Dong, F., Directional electron delivery via a vertical channel between g-C_3N_4 layers promotes photocatalytic efficiency. *J. Mater. Chem. A* **2017,** *5*, (19), 9358-9364.

564